Characterization of two-way fabricated hybrid metal-oxide nanostructured electrode materials for photovoltaic and miniaturized supercapacitor applications

S.A. Adewinbi[a,b,c], B.A. Taleatu[b],*, V.M. Maphiri[c], O. Fasakin[b,c], E .Omotoso[b], K.O. Oyedotun[c] and N. Manyala[c]

[a]Department of Physics, Osun State University, Osogbo, Osun State, 210001, Nigeria
[b]Department of Physics and Engineering Physics, Obafemi Awolowo University, Ile-Ife, 220005, Nigeria
[c]Department of Physics, Institute of Applied Materials, SARChI Chair in Carbon Technology and Materials, University of Pretoria, Crn Lynnwood and University Road, Hatfield, Pretoria, 0002, South Africa

*Corresponding author. bdntaleatu@oauife.edu.ng

Highlights

- Three different thin film-based structures (Co_xO_y, MoO_3, and V_2O_5) were prepared by electrochemical deposition.
- Photovoltaic measurements were carried out on the fabricated solar cells under illumination.
- Half-cell and symmetric full cell electrodes were fabricated for energy storage application.
- Electrochemical reactions were investigated to understand energy storage capabilities of the electrodes.

Graphical abstract

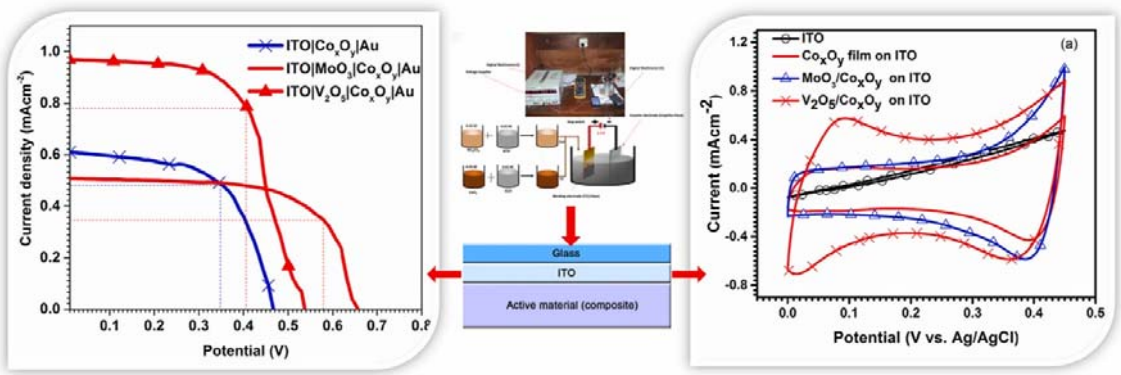

Abstract

Portable electronic devices require a small volume self-powered energy system that can combine fabrication of energy harvesting and storage devices in one plane. This study focuses on fabricating novel all-oxide photovoltaic and supercapacitor devices based on MoO_3, V_2O_5, and Co_xO_y thin electrodes prepared by a two-electrode cell arrangement. The fabricated devices were tested using solar simulator and potentiostat at ambient temperature. The power conversion efficiencies of the fabricated photovoltaic devices were found in the range of 0.17–0.39% depending on buffer layer characteristics. It therefore suggests that V_2O_5 and MoO_3 can buffer photovoltaic processes by lowering the conduction band offset in the proximate Co_xO_y absorber. Pseudocapacitive behavior of $MoO_3/Co_xO_y||MoO_3/Co_xO_y$ and $V_2O_5/Co_xO_y||V_2O_5/Co_xO_y$ planar devices showed that they delivered maximum specific areal capacity values of 0.694 and 0.778 μAhcm^{-2} respectively at discharge current density of 0.1 mAcm^{-2}. They also showed considerably low reduction in energy density (about 38.7%) even at a remarkable increase in power density of about 450% (at a high current density of 1.0 mAcm^{-2}). In addition, the symmetric microsupercapacitors showed excellent retention of capacity

even after 5000 cycles. These results generally indicate the reliability of the fabricated devices in the development of portable electronic components for energy application.

Keywords: Metal oxide; Photovoltaic; Microsupercapacitor; Power conversion efficiency; Areal capacity

1. Introduction

The release of greenhouse gases from fossil fuels and its recent form of depletion have necessitated the involvement of alternative and renewable energy sources that are free of these hazardous components. Amongst these renewable energy sources is solar energy generated photovoltaic technology [1]. However, this energy source is sometimes not available due to weather condition. It is available only during the day resulting in some challenges on the effectiveness of the photovoltaic (PV) system. To overcome some of these challenges, energy storage devices are used to effectively store energy captured during the day [[1], [2]]. These storage devices are in different categories which include conventional capacitors, batteries and supercapacitors [3]. Micro batteries have received much attention as a potential resolution but they still suffer some setbacks such as relatively low power densities and short-term cycle stability as a result of high volumetric electrochemical reactions [4,5]. Development of microsupercapacitors (μ-SCs) with a view to incorporating it into microbatteries and light harvesting devices for good performance and maximum power as a single unit of energy management system is underway [4]. Although, various thin film compounds have been used for these purposes, some of them are costly due to their deposition processes while some are not environmentally friendly. However, some transition metal oxide based materials have been found useful because of their multifunction capabilities [3]. Their unique varying and tuneable optical properties enable them a major role in photovoltaic process such as light harvesting, charge extraction, transport and so on. Nevertheless, silicon and some III-V semiconductors have historically received much attention, only few metal oxides have been specifically investigated as photon absorber [2,3]. But recently, many emerging oxides are being investigated. *n*-type metal oxide semiconductors are utilized either as transparent conducting front contacts, electron (and hole) transport layers that give the required charge selectivity between the absorber and the contacts, or as back contact electrodes [[3], [6], [7]]. Typically, some metal oxides have several redox states or structures that contribute to charge storage in pseudocapacitors via fast redox reactions [8]. For example, RuO_2 has shown remarkable performance in supercapacitors (exhibiting the relatively high specific capacitance values of 720 Fg^{-1}) and stimulated many interests in investigating metal oxide systems for supercapacitor application [9]. The electrochemical measurements of a fabricated symmetric μ-SC from electrodeposited ordered mesoporous RuO_x showed strong capacitive properties with a maximum specific capacity of 12.5 $Whkg^{-1}$ and areal capacitance of 2.6 $mFcm^{-2}$ based on the deposited material density [10]. Although, other simple metal oxides such as MnO_2, Co_3O_4, NiO, SnO_2, Fe_3O_4, and V_2O_5 have been employed as electroactive materials for pseudocapacitors, they usually have some limitations such as poor electrical conduction, insufficient electrochemical cycling stability, limited potential operating window and low specific capacitance [8,11]. Mixed binary or ternary metal oxides systems, such as Ni, Mn, Co, Fe, Ti, Sn, Al or Cu based mixed oxides have shown improved properties as electroactive materials for pseudocapacitors [11]. Electrochemical capacitors dependent on Co-oxide have also shown excellent capacity but their practical application in supercapacitors is hampered by its poor conductivity [8]. In order to improve the electrical conductivity, a common approach of mixing Co-oxide with more conducting material is required [7]. For the purpose of this study, the authors have designed a cheap route of producing hybrid oxide structures capable of effective light absorption, charge transport and pseudocapacitive properties. They are composed of interfacial layers built from cobalt oxide with orthorhombic molybdenum oxide (α-MoO_3) and vanadium oxide nanoparticles (α-V_2O_5) separately on indium tin oxide coated glass (ITO) substrate. The ITO also served as conducting layer through the current needed for both photovoltaic and electrochemical charge storage processes is tapped. This is with a view to

developing all-in-one energy system incorporating eco-friendly metal oxide framework and utilizing the stable fabrication technology of Axi patterning and scalable electrochemical deposition process for large scale development. To our knowledge, this study is being reported for the first time. Some surface properties of these structures have been investigated in one of our previous studies and the results showed that they are suitable and scalable materials for device fabrication [12].

2. Materials and methods

Necessary reagents, growth procedures and sample testing are described concisely in the following sub-sections.

2.1. Preparation of the metal oxides thin films

MoO_3, V_2O_5 and Co_xO_y thin solid films were electrodeposited by a home made two electrode cell arrangement on ITO coated glass substrates of dimension (20 × 15 × 0.7) mm and 15 Ω/m^2 surface resistivity obtained from Lumtec Incorporation. Thin films of MoO_3 and V_2O_5 were grown from the electrolyte prepared from 0.05 M of $(NH_4)_6Mo_7O_{24(aq)}$ and 0.05 M of NH_4VO_3 with 0.01 M KOH(aq) respectively while Co_xO_y film was deposited from standard electrolytic solution comprising 0.01 M of $CoCl_{2(aq)}$ and 0.01 M of KOH.

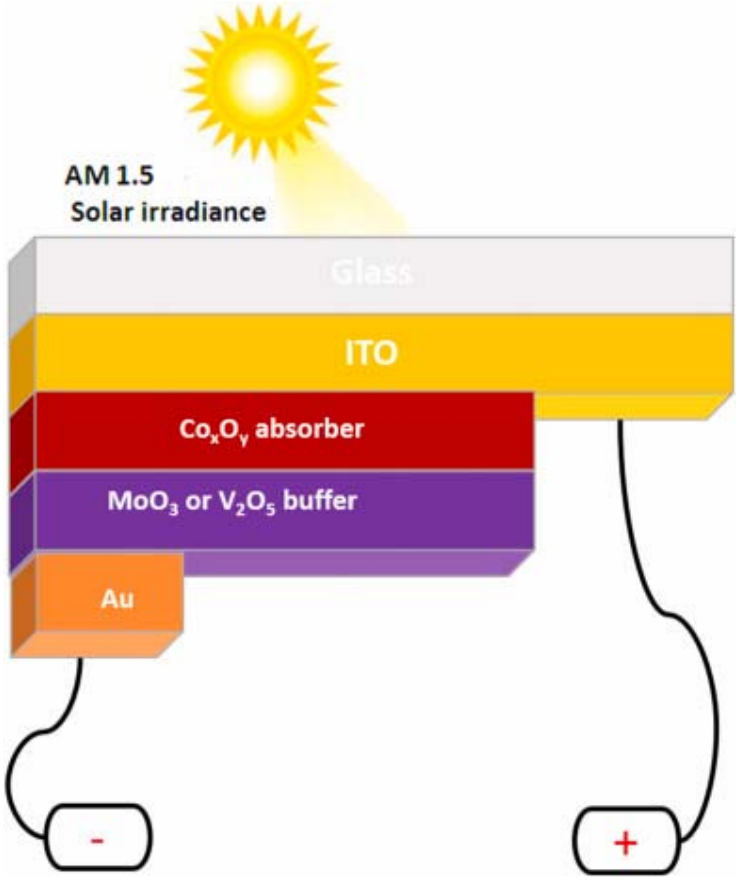

Fig. 1. Schematic structure of fabricated PV.

2.2. Photovoltaic cells fabrication and measurements

Three photovoltaic cell prototypes were fabricated using superstrate configuration. In this configuration, light enters the cell through the anode (ITO/glass). Two different films, MoO_3 and V_2O_5, were first separately deposited onto ITO substrates as buffer. Co_xO_y absorber layer was electrochemically deposited onto them separately [12]. Each layer was subjected to heat treatment in furnace at temperature of 300 °C to remove adsorbed impurities. After the growth of these layers, gold (Au) contacts were fabricated on them as front contact with the aid of resistive evaporation technique. Thus, two different samples were produced and they are represented using the schematic shown in Fig. 1. Cell without buffer was also fabricated as control sample. Current density-voltage (*J-V)* measurement of the cells was carried out under standard test condition using a solar simulator (Model 91150V) under 100 mW/cm^2 solar output at ambient temperature and AM1.5 G reference spectra filtering. This was with a view to providing the fingerprints of the fabricated PV devices.

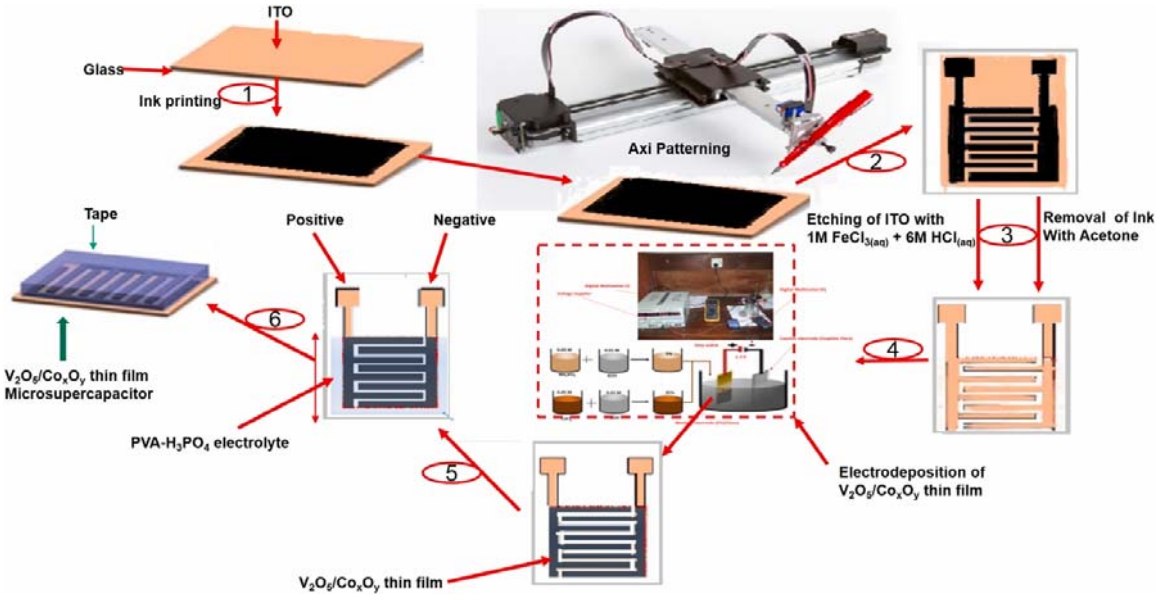

Fig. 2. Fabrication process of the MoO_3/ Co_xO_y || MoO_3/ Co_xO_y and V_2O_5/ Co_xO_y || V_2O_5/ Co_xO_y Symmetric µ-SCs.

2.3. Fabrication of MoO_3/Co_xO_y and V_2O_5/Co_xO_y based electrodes and symmetric µ-SCs

Half-cell electrodes and full cell devices of each of MoO_3/Co_xO_y and V_2O_5/Co_xO_y structures were prepared. The half-cells were obtained by depositing MoO_3/Co_xO_y and V_2O_5/Co_xO_y separately onto the unpatterned ITO substrates according to the steps in section 2.2. In this case, there was no evaporation of gold front contact. Fig. 2 shows the schematic representation of stages in the fabrication of the full-cell planar micro-supercapacitors. Two pieces of ITO coated glass substrates were first patterned by masking and imprinting with a separation of about 1.5 mm to serve as current collector. The patterning tool is an Axi drawer. Then, the patterned substrates were dipped in a solution comprising 1 M of Iron (III) chloride ($FeCl_3$) and 6 M of hydrochloric acid (HCl) for etching of unmasked region for about 5 min. They were thereafter rinsed with deionized water (DI). The mask was removed by acetone and then rinsed with DI water. Afterwards, the film structures (MoO_3/Co_xO_y and V_2O_5/Co_xO_y) were electrodeposited on the etched patterned ITO/glass substrates. Desired area (1 by 1 cm^2) of the film was coated with PVA/KOH (poly vinyl alcohol/potassium hydroxide; weight ratio 1:1 in 20 ml of DI water) gel polymer electrolyte. Each cell was covered with transparent Kapton tape to prevent wrinkling of the polymer gel layer and adsorption of airborne impurities. They were

then dried for 6 h in oven to remove any suspecting water content at temperature of about 110 °C. Thus, the full cell planar devices (μ-SCs) are obtained. The supercapacitive properties of both fabricated half-cell electrodes and full cell devices were tested using a Bio-Logic VMP300 potentiostat (Knoxville TN 37,930, USA) incorporated with EC-Lab® V1.40 software. The deposited films were the working electrodes while the glassy carbon (graphite piece) and Ag/AgCl served as counter and working electrodes respectively. The measurements were conducted in a 1.0 M concentration of KOH solution electrolyte at potential window 0–0.45 V in ambient environment.

3. Results and discussion

3.1. I–V characteristics of the PV cells

Solar cells parameters deduced from current density-voltage (*J-V)* curves (shown in Fig. 3) are presented in Table 1. These are short circuit current (J_{SC}) and open circuit voltage (V_{OC}). The closeness of solar cell *J-V* curve to rectangular shape gives the fill factor (*FF*) of the cell. The Fill factor and cell's efficiency, η, were calculated from Eqs. (1), (2) accordingly [13].

$$FF = \frac{V_{max} I_{max}}{V_{oc} I_{sc}} \tag{1}$$

$$\eta = \frac{V_{oc} I_{sc} FF}{P_{light}} \tag{2}$$

where, P_{light} is the power density of the AM 1.5 spectrum ($100\ mW cm^{-2}$). Shunt R_{SH} and series R_S resistances were determined from the slopes of the curves near short circuit current density and open circuit voltage with respect to the expressions in Eqs. (3), (4) below [13,14].

$$R_{SH} = -\frac{\Delta V}{\Delta I}\ at\ V = 0 \tag{3}$$

$$R_S = -\frac{\Delta V}{\Delta I}\ at\ V = V_{OC} \tag{4}$$

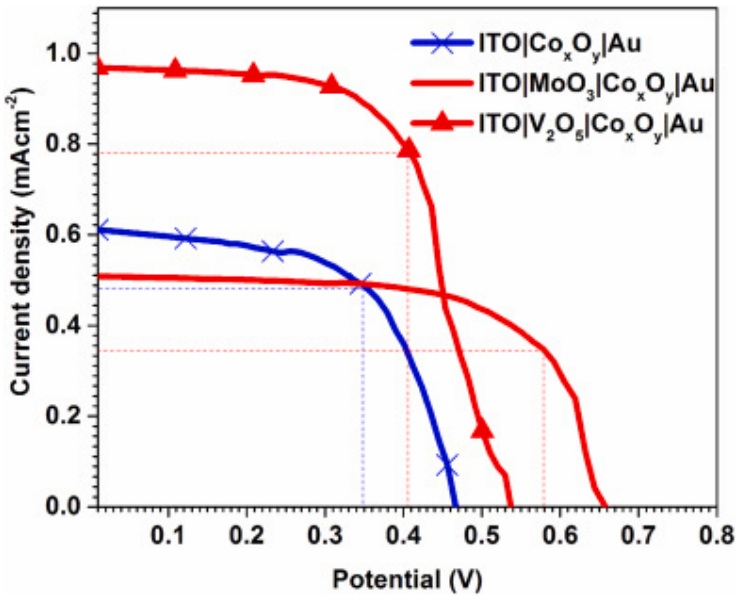

Fig. 3. I–V curves of the metal oxide PV cells under AM1.5 solar illumination.

Table 1. Photovoltaic parameters of the fabricated solar cell structures.

S/n	Samples	V_{OC} (V)	J_{SC} ($mAcm^{-2}$)	*FF* (%)	RS ($\Omega\ cm^2$)	R_{SH} ($\Omega\ cm^2$)	η (%)
1	ITO/Co_xO_y/Au	0.46	0.620	58.91	193.25	357.1	0.169
2	ITO/MoO_3/Co_xO_y/Au	0.66	0.495	62.14	141.03	402.6	0.203
3	ITO/V_2O_5/Co_xO_y/Au	0.54	0.950	92.47	138.18	454.4	0.390

The low *J-V* response of all the cells could be attributed to the small shunt resistance (<1000 Ω) and high series resistance of the cells (>100 Ω). The high series resistance could be related to middle contact electron traps probably due to insufficient adherence of electrode contacts to the cells while the low shunt resistance can be linked to short circuiting that could have arisen from the cells coupling. It could also be attributed to mechanical and vibrational modes which emanate from micro-cracks, defects or potential induced degradation caused by localized shunt. All these irregularities reduce R_{SH} values [14]. The ITO/Co_xO_y/Au led to a current density of 0.62 $mAcm^{-2}$ and a low open circuit potential of 0.46 V. With the amalgamation of the MoO_3 and V_2O_5 buffer layers, V_{OC} increases notably to 0.66 and 0.54 V, respectively. Increase in the values of shunt resistance indicates that the cells performance can be enhanced by buffer layers. Similar observations were already reported for ITO|TiO_2|Co_3O_4 cells [15]. In addition, series resistance of the MoO_3 based cell is considerably higher than the one built with V_2O_5 buffer layer. This suggests higher potential barrier for electrons in the MoO_3 buffer. Current density of 0.495 mA/cm^2 is also lower compared to that of ITO|Co_xO_y|Au cell. Highest value of cell efficiency (0.39%) was obtained with V_2O_5 buffer layer although its open circuit potential (0.54 V) was considerably lower than that of ITO|MoO_3|Co_xO_y|Au cell. The high cell efficiency suggests an improved heterojunction interface compared to ITO/Co_xO_y/Au and ITO/MoO_3/Co_xO_y/Au cells. A combined TiO_2|Co_3O_4|MoO_3 all oxide heterojunction photovoltaic device involving TiO_2 buffer, Co_3O_4 absorber and MoO_3 hole selective contact investigated by Majhi, and co-workers [16] yielded lower efficiency (0.16%) than our observation. From PV performance values in Table 1, the obtained V_{OC} is notably large. This may stem from various challenges such as the control of defect or impurity density at the heterojunction, or the texture of the absorber [6,14,15].

3.2. Electrochemical characterization of Co_xO_y film and half-cell electrode

The electrochemical properties of the annealed films are studied under a three-electrode cell setup.

3.2.1. Cyclic voltammetry (CV)

The *CV* curves of blank ITO substrate, Co_xO_y film and the bilayer half-cell electrodes are presented in Fig. 4. A look at the curves in Fig. 4(a) shows that the current response of blank ITO is very negligible compared to the grown samples. Also, comparative studies of the *CV* curves of proximate Co_xO_y film as well as MoO_3/Co_xO_y and V_2O_5/Co_xO_y bilayer electrodes measured under the same potential window and scan rate (5 mVs^{-1}) were done to understand their supercapacitive behavior. It is clearly shown from the curves that upon introducing MoO_3 and V_2O_5 on the spinel Co_xO_y film to form separate Co–Mo and Co–V oxides electrodes, the structures exhibit higher current response compared to the pure Co_xO_y layer suggesting higher specific capacity [17]. The areas under the bilayer curves are also relatively large. Hence, it can be inferred that the bilayer structures have better capacitance because high current response contributes to high specific capacitance of the material [17,18]. The large curved surface area could also signify high specific capacitance since more active sites possess the capability of giving multiple redox reaction [19]. The contributions of both MoO_3 and V_2O_5 overlayers can be explained by the formation of their thin nanoparticles on the Co_xO_y underlayer which increase its surface area and therefore enhance the capacitive responses [12,20]. CV curves of MoO_3/Co_xO_y and V_2O_5/Co_xO_y bilayer electrodes at scan rates ranging from 5 to 100 mV/s are presented in Fig. 4(b) and (c), respectively. Two distinct pairs of reversible redox (anodic and cathodic) peaks were also observed from the curves. The appearance of these peaks suggests battery type behaviors of the electrodes [21]. The redox peaks which became more defined at higher scan

rates can be associated to Co(II)/Co(III) or Co(III)/Co(IV) and Mo (VI) or V (V) redox processes [19,22,23]. These processes can be ascribed to intercalation or de-intercalation of OH^- or K^+ into the matrix of the electrode films. Reversibility is also observed in these redox peaks. This reversibility has been reported as an indication of redox mechanism being diffusion controlled with linear increase in both anodic and cathodic peaks [18]. Similar curve has been reported for a mesoporous (Co_3O_4) film by Lee and coworker [24]. Thus, the redox peaks contribute to the oxidation and reduction of cobalt compound which can simply be explained by the chemical reactions:$Co_3O_4 + OH^- \rightarrow 3CoOOH + e^-$ (0.1–0.2 V)$CoOOH + OH^- \rightarrow CoO_2 + H_2O + e^-$ (0.3–0.4 V)

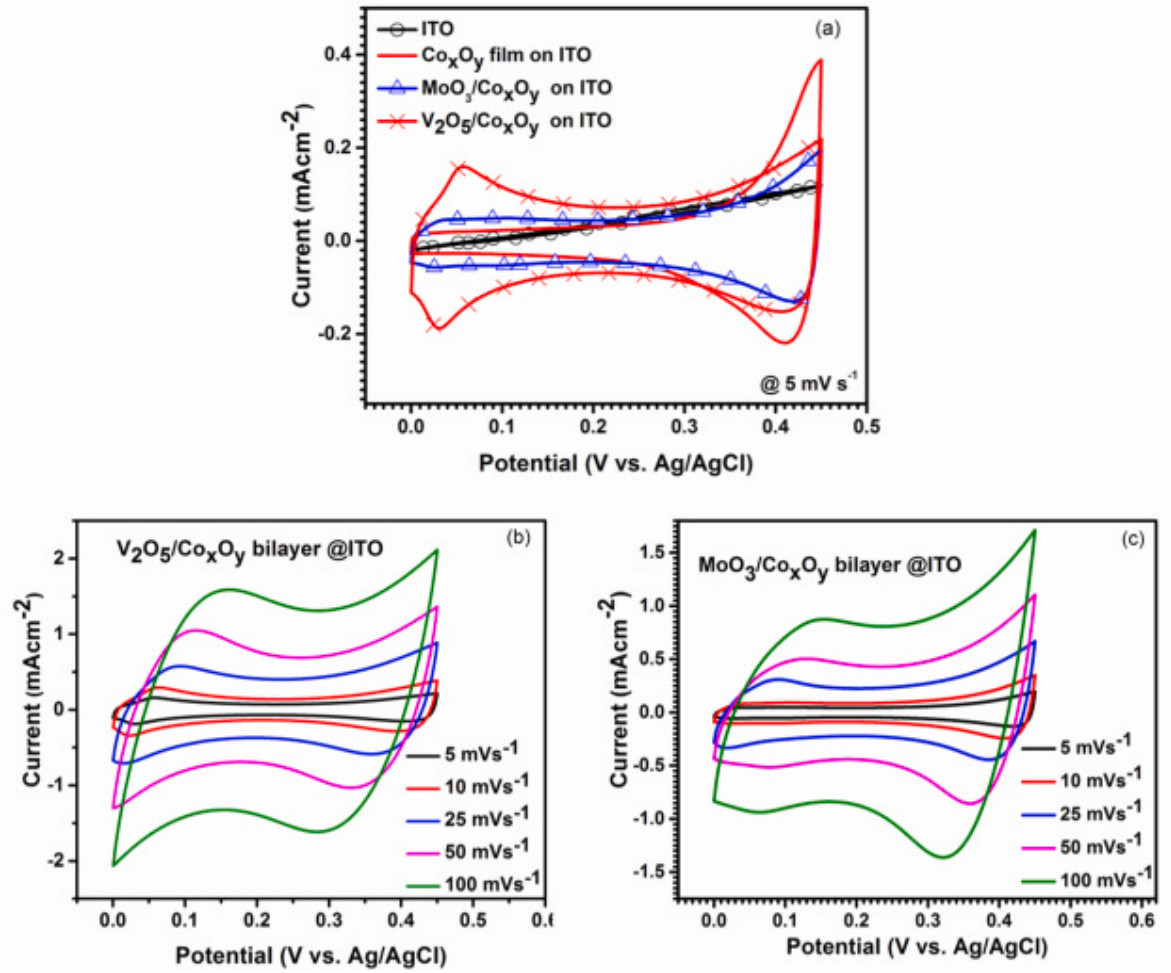

Fig. 4. CV curves of Co_xO_y film, V_2O_5/ Co_xO_y and MoO_3/ Co_xO_y bilayers at a scan rate of 25 mVs−1 (b) the CV curves of V_2O_5/ Co_xO_y bilayer only at various scan rates.

From the reactions above, there was a reduction of Co_3O_4 to CoOOH in the potential window of 0.1–0.2V vs Ag/AgCl which thereafter oxidizes to CoO_2 in range 0.3–0.4 V. This reversibly then brings it to Co_3O_4 at all the corresponding potential windows [24]. Other mechanisms attributable to the redox peaks are:

$$\alpha - \mathrm{MoO_3} + x\mathrm{K^+} + x\,\mathrm{e^-} \leftrightarrow \mathrm{K}_x\mathrm{MoO_3}$$

$$\alpha - \mathrm{V_2O_5} + x\mathrm{K^+} + x\,\mathrm{e^-} \leftrightarrow \mathrm{K}_x\mathrm{V_2O_5}$$

The observable redox peaks also show that the electrochemical properties of the electrodes are not that of electric double layer capacitance (EDLC) but Faradaic redox reaction [19]. The *CV* curves also revealed a very sharp current peak at the terminal part of the potential (0.45 V). These characteristics have been reported as an indication of oxygen evolution reaction (OER) signifying electrocalalytic effect [18]. From the curves, it can also be seen that the shape of the curves was constant at higher scan rates. The area under the curves for both forward and reverse scanning also increases. The increase in scan rates also led to a normalized *CV* curves with current response increasing in the same order of magnitude. This suggests a good response of the half cells [18] and also corroborates occurrence of a fast ion transfer process [20]. The Areal capacitance C_a of all the electrode materials at 5 mVs^{-1} are calculated from the CV curves (Fig. 4(a)) in accordance to the relation below;

$$C_a = \frac{1}{AS_r.V}\int_{v_1}^{v_2} IdV_s \ \ (mFcm^{-2}) \tag{5}$$

where, v_1 and v_2 are the initial and final peak potentials of the potential window, I is the integral current response (mA) of the curves, V is the cell potential (V) for the electrode, S_r is the scan rate (mVs^{-1}) and A is the area of loading electrode material dipped in the electrolyte (cm^2) of the single electrode [17,18]. The C_a values at the lowest optimized scan rate 5 mVs^{-1} for Co_xO_y, MoO_3/Co_xO_y and V_2O_5/Co_xO_y electrode films are calculated as 19.44, 25.11, and 42.22 $mFcm^{-2}$, respectively.

3.2.2. Galvanostatic charge discharge (GCD)

The GCD measurement of the half-cell electrodes was conducted to sufficiently understand the supercapacitive properties of the electrode films. The curves are presented in Fig. 5. Comparative studies of charge-discharge capabilities of the Co_xO_y single layer and the two bilayer half-cell electrode films are shown in Fig. 5(a). From the curves, it can be observed that, the bilayer film electrodes generally exhibit longer discharge time compared to the Co_xO_y single layer half-cell. It is also noticed that V_2O_5/Co_xO_y electrode exhibited relatively longer discharge period than the corresponding thicker MoO_3/Co_xO_y. This implies that vanadium significantly improves the pseudocapacitance of the Co_xO_y layer than molybdenum. It also corroborates its relative larger area in the CV curves earlier observed. Also, it can be seen that the CD curves of the two bilayer half-cell electrodes are not linear. Careful examination of the discharge cycle of the curves revealed three special varying regions. First, there exists a sudden drop in current at the onset of the discharge. This drop can be due to electrode internal resistance. The internal resistance R_i is calculated from the relation,

$$R_i = \frac{IR_{drop}}{2AI_{cons}} \tag{6a}$$

where IR_{drop} is the voltage drop at the onset of the discharge side, I_{cons} is the applied current and A is the area of the active sites of the electrode films [18].

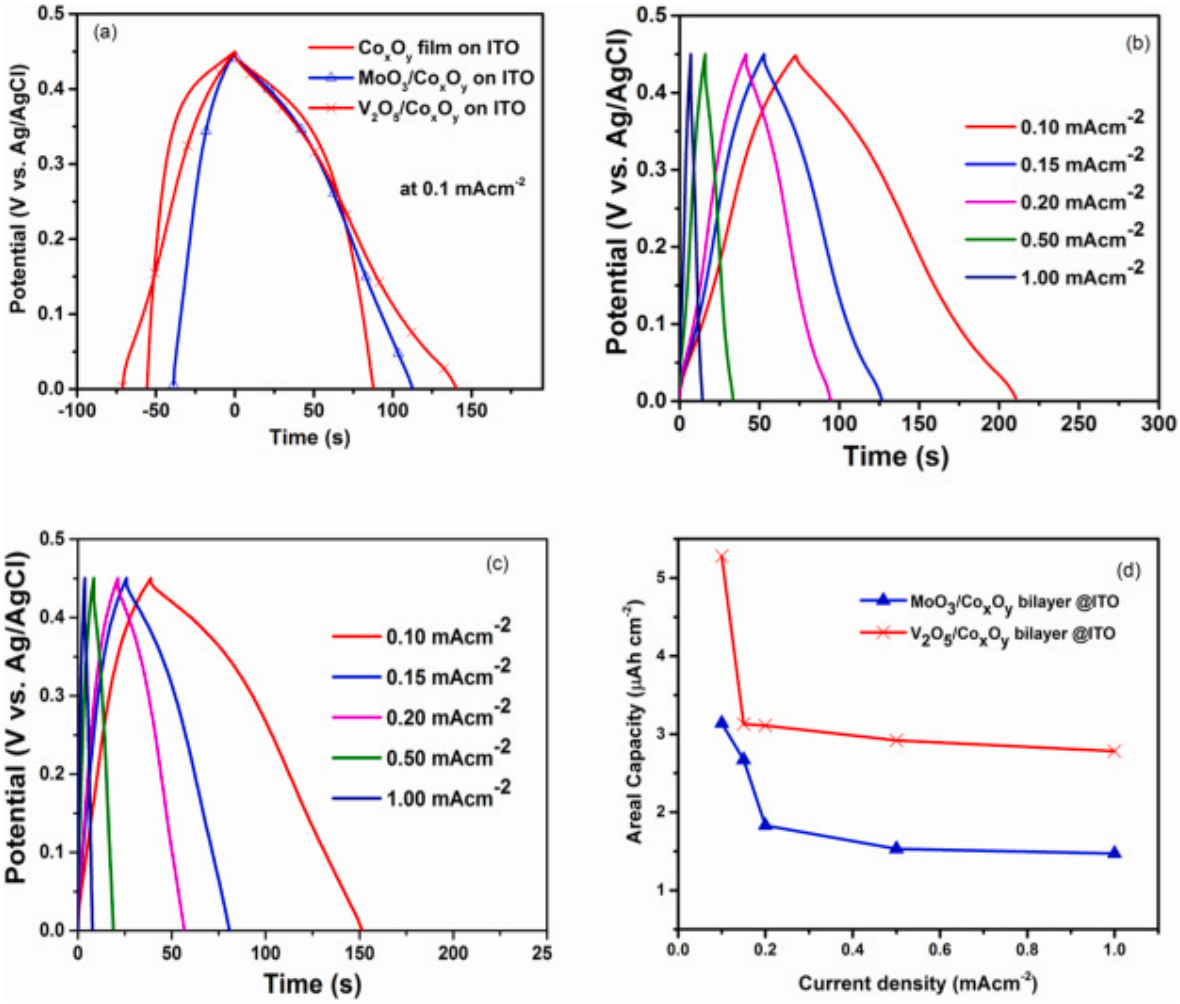

Fig. 5. CD curves of (a) Co_xO_y film, V_2O_5/ Co_xO_y and MoO_3/ Co_xO_y bilayers at a current density of 0.1 mAcm-2 (b) V_2O_5/ Co_xO_y bilayer at various current densities (c).

The values of R_i are estimated as 1.17, 1.24 and 1.87 Ω for Co_xO_y, MoO_3/Co_xO_y and V_2O_5/Co_xO_y electrodes respectively from the CD curves at 0.1 mAcm^{-2}. The results show that the V_2O_5/Co_xO_y electrode has higher internal resistance than both the single layer Co_xO_y and MoO_3/Co_xO_y. Second, the non-linear portion which is the slope dependence of the potential can be attributed to redox characteristics which suggest faradaic behavior of the electrodes. It corroborates the results of the CV study. The third region illustrates the linear variation of the potential-time relation which is a feature of double layer characteristics [5,18].

The Areal capacity Q_a of all the electrode materials is calculated using the slope of their discharge cycles from the relation in Eq. (6b).

$$Q_a = \frac{I_d \times \Delta t}{3.6} \ (\mu Ahcm^{-2}) \tag{6b}$$

where I_d is the current density in Amperes per square centimeter unit area A (mAcm^{-2}) and Δt is the electrode discharge time measured in seconds [17]. The values of Q_a at current density 0.1 mAcm^{-2} are estimated as 2.43, 3.14 and 5.28 μAhcm^{-2} for Co_xO_y, MoO_3/Co_xO_y, and V_2O_5/Co_xO_y electrodes respectively. To investigate the effect of varying applied current densities, the GCD of the electrodes was conducted at current densities of 0.10, 0.15, 0.20, 0.50, and 1.00 mAcm^{-2} in the potential window

ranged from 0 to 0.45 V versus Ag/AgCl. The curves of the two bilayer electrode films are shown in Fig. 5(b and c). The calculated areal capacities of the electrodes are plotted against the selected current densities (Fig. 5(d)). From the plots, it can be observed that areal capacities of electrodes are a function of current density; they decrease with increase in current densities. This means that at low current densities, the electrolyte ions and the electrons were able to access the reaction sites at the electrodes' interior. But the charge diffusion seems to be impeded and the redox process at the electrode/electrolyte interface took place within a short period of time, hence only surface reactions took place at higher current densities. This in turn leads to decrease in capacity values as the current density increases [17,18]. Comparing the two bilayer electrode films, it is observed that V_2O_5/Co_xO_y electrode gave higher C_a and Q_a than the corresponding MoO_3/Co_xO_y and Co_xO_y single layer electrodes. Its relative higher values can be ascribed to synergistic interaction of the films with the substrate as well as the porous nature of the electrode films. This mesoporous feature can allow more diffusion pathways and expose the electrolyte to more active sites. It can also ease intercalation/deintercalation of ion into the electrode matrix [12,17]. Fig. 6 illustrates the stability test of the two bilayer half-cell electrodes. The figures show the specific capacity retention and energy efficiency as a function of cycle number (2000 charge-discharge cycles). The two mixed oxides demonstrated retention close to the initial 100% up to the 300th cycle and about average of 60 and 65% of their initial areal capacities at 2000 cycles. Coloumbic efficiencies of about 93.3 and 95.8% from the 400th to the 2000th cycle for MoO_3/Co_xO_y and V_2O_5/Co_xO_y half-cell electrodes are also realized respectively. In addition, the stability of the V_2O_5/Co_xO_y electrode film is relatively better than that of MoO_3/Co_xO_y film. The difference can be likened to lower internal resistance offered by V_2O_5/Co_xO_y bilayer electrode [18]. These results therefore show that the Co–V mixed oxide electrode has the capability of offering better capacitive values and higher stability than Co–Mo. The higher stability of the oxide could be ascribed to enhanced interaction and adherence of the oxides layers to the substrate while the high capacity retentions could be ascribed to the higher electronic conductivity as a result of low R_s value [17]. In addition, the porous and stacked flake-like structure of the V_2O_5/Co_xO_y layer can enhance ion diffusion [12]. Generally, all the electrodes show appreciable stability to be applied in supercapacitor.

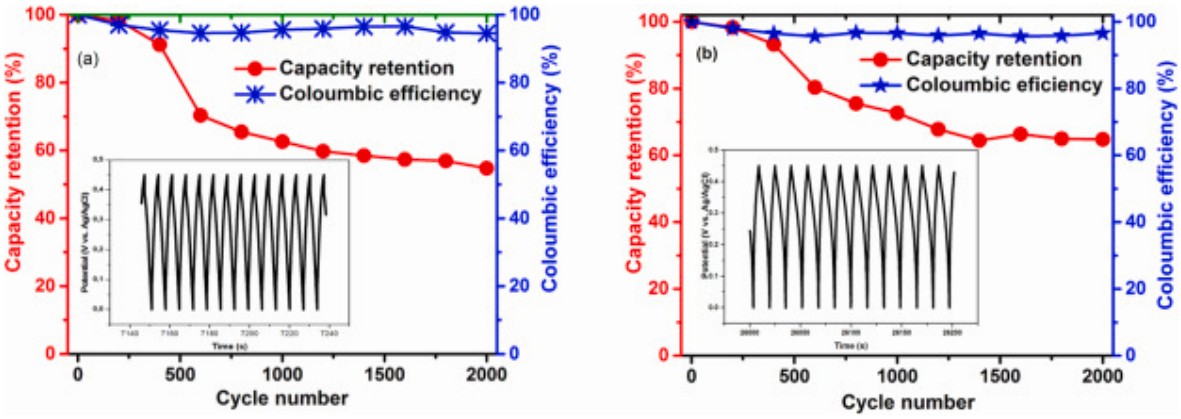

Fig. 6. (a and b) Variations of specific capacity and energy efficiency of V_2O_5/ Co_xO_y and MoO_3/ Co_xO_y bilayer thin film electrodes as a function of cycle.

3.2.3. Electrochemical impedance spectroscopy (EIS)

The EIS studies of the Co_xO_y thin film and the bilayer electrodes (MoO_3/Co_xO_y and V_2O_5/Co_xO_y) were conducted under the same electrochemical condition. Nyquist plots derived from the measurements are represented in Fig. 7. From the plots, deviation from perpendicularity is clearly noticed. This confirmed the pseudocapacitance properties of the electrodes with reference to the fact that EDLC electrodes exhibit curves parallel to the imaginary impedance (y-axis) or perpendicular to the real impedance (x-axis). Values of series resistances R_s of each sample are determined from the plots as 28.25, 21.30 and 18.47 Ω/cm^{-2} for Co_xO_y, MoO_3/Co_xO_y and V_2O_5/Co_xO_y, respectively. R_s

value has been reported as feature that significantly influences the C_a and Q_a of electrode structures [17].

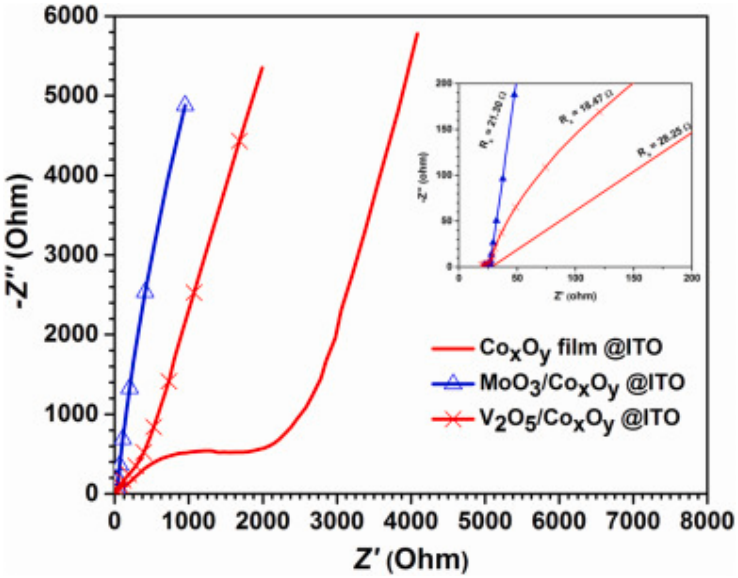

Fig. 7. EIS Nyquist impedance plot of Co_xO_y film, V_2O_5/ Co_xO_y and MoO_3/ Co_xO_y bilayers electrodes (Inset: Nyquist plots at low frequency region with Z′ and Z″ in range.

3.3. Electrochemical characterization of fabricated full cell μ-SCs

Electrochemical behavior of the two fabricated symmetric supercapacitor cells was investigated. The observations are presented as follows.

3.3.1. Cyclic voltammetry (CV)

The CV measurements of the $MoO_3/Co_xO_y||MoO_3/Co_xO_y$ and $V_2O_5/Co_xO_y||V_2O_5/Co_xO_y$ fabricated symmetric μ-SC devices were taken at scan rates in the range of 5–100 mVs^{-1} with PVA/KOH polymer gel electrolyte. The resulting CV curves are presented in Fig. 8(a and c). The CV curves of the two planar μ-SCs show shapes with slightly broad redox peaks at scan rate of 5 mVs^{-1}, revealing the pseudocapacitance properties of the samples with respect to Faradaic reactions that occur at the surface/bulk composition of the thin film [25]. This feature constitutes the redox reactions of the electrodes attributed to the insertion/de-insertion processes of OH^- within the two similar thin film electrodes. At higher scan rates, it is obvious that the initial shape deforms and the CV curves of the devices tend toward rectangular shape. In addition, it can be seen that the CV curves of the symmetric $MoO_3/Co_xO_y||MoO_3/Co_xO_y$ and $V_2O_5/Co_xO_y||V_2O_5/Co_xO_y$ supercapacitors slightly deviated from those of their half-cell electrodes. This could signify a restriction to the energy storage performance of the devices. Makino and colleagues (2013) attributed similar feature to low conductivity of the materials which retards faradaic reactions and consequently limits the charge/discharge rate of the devices [10].

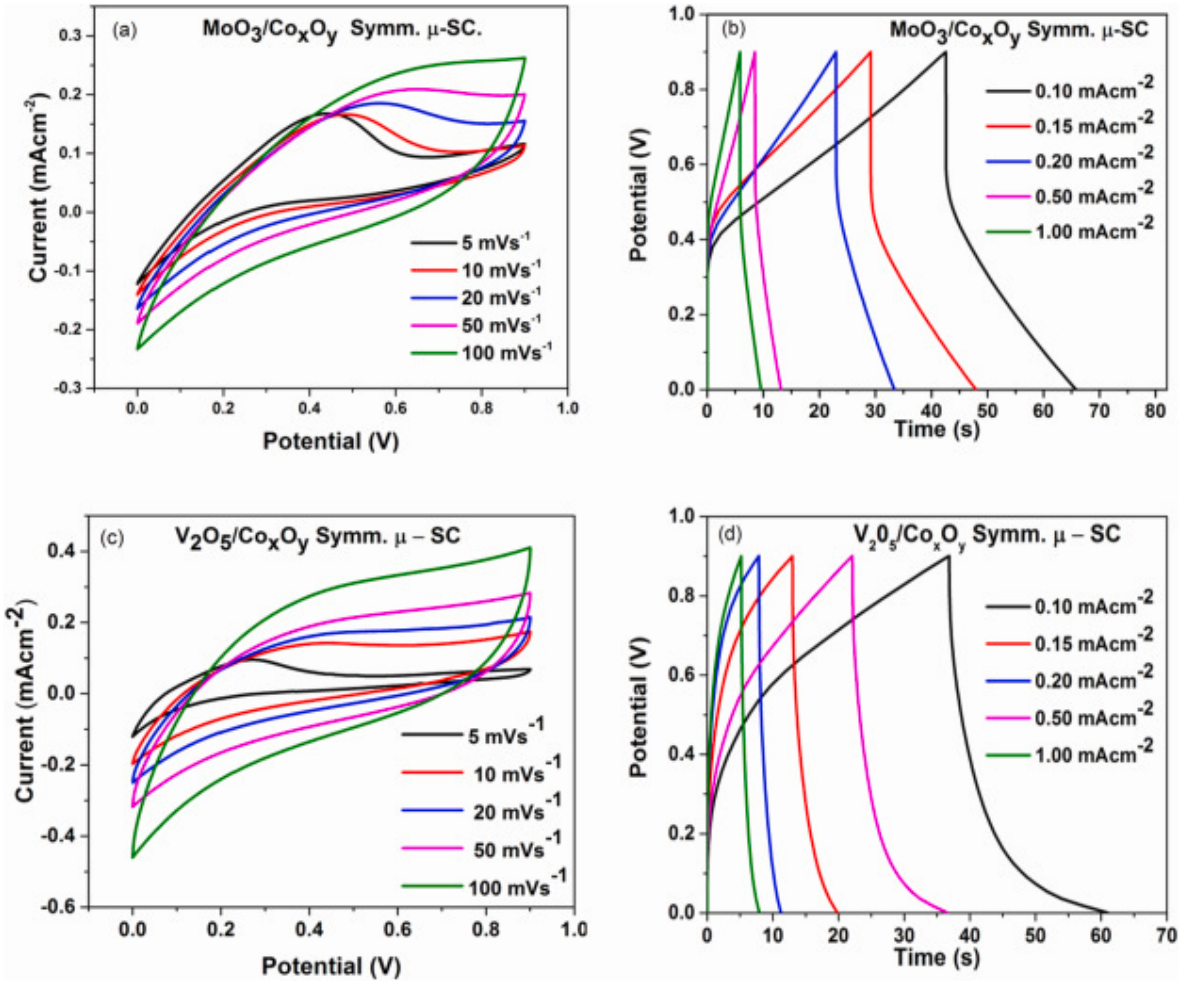

Fig. 8. (a and c) CV curves of MoO_3/ Co_xO_y || MoO_3/ Co_xO_y and V_2O_5/ Co_xO_y || V_2O_5/ Co_xO_y fabricated symmetric microsupercapacitor at different scan.

3.3.2. Galvanostatic charge/discharge (GCD)

The GCD potential of the fabricated supercapacitor cells was also studied to evaluate their energy storage capability. This is demonstrated by the CD curves of the $MoO_3/Co_xO_y||MoO_3/Co_xO_y$ and $V_2O_5/Co_xO_y||V_2O_5/Co_xO_y$ planar μ-SCs shown in Fig. 8(b and d). The curves display a near symmetric non-ideal triangular shape. This feature implies a charge/discharge pattern of battery materials with partial capacitive behavior (pseudocapacitance), found to be similar to the newly termed supercapattery device [17,23,26]. Therefore, it can be deduced that both the $MoO_3/Co_xO_y||MoO_3/Co_xO_y$ and $V_2O_5/Co_xO_y||V_2O_5/Co_xO_y$ planar architectures can possess the capabilities of combining high-power rated supercapacitors and capacious charge storage functions of a battery (supercapattery) [26]. Areal capacitance (C_a) and capacity (Q_a) values of the supercapacitors were also calculated from galvanostatic charge/discharge curves, accordingly. The calculated values show that the $MoO_3/Co_xO_y||MoO_3/Co_xO_y$ and $V_2O_5/Co_xO_y||V_2O_5/Co_xO_y$ planar devices show maximum areal capacitance values of 2.78 and 3.11 $mFcm^{-2}$ and capacity values of 0.694 and 0.778 $\mu Ahcm^{-2}$ at 0.1 $mAcm^{-2}$ discharge current density respectively. These values compare well and showed improvement with some reports on μ-SCs in literatures [5,[25], [26], [27]]. Plots shown in Fig. 9(a) illustrate the calculated areal capacitances/capacities as a function of applied charge/discharge current densities. Similar to the feature reported for their respective half-cell electrodes, diminutions were observed in their capacitances and capacities at higher current densities. It has also been reported that at high current density, transfer of ions is restricted only to outer surface

of electrodes due to insufficient time and thus lowers the capacitance value of the device [18]. Energy density E_d and Power density of the planar micro-supercapacitor prototypes were calculated from the GCD curves according to following equations;

$$E_d = {}^{I}/_{3.6A} \times \int V dt \ (mWhcm^{-2}) \tag{12}$$

$$P_d = \frac{E_d}{\Delta t} \times 3600 \ (mWcm^{-2}) \tag{13}$$

where V is the operating potential (V), I is the discharge current (mA cm^{-2}) of the device and Δt is the discharge time [26].

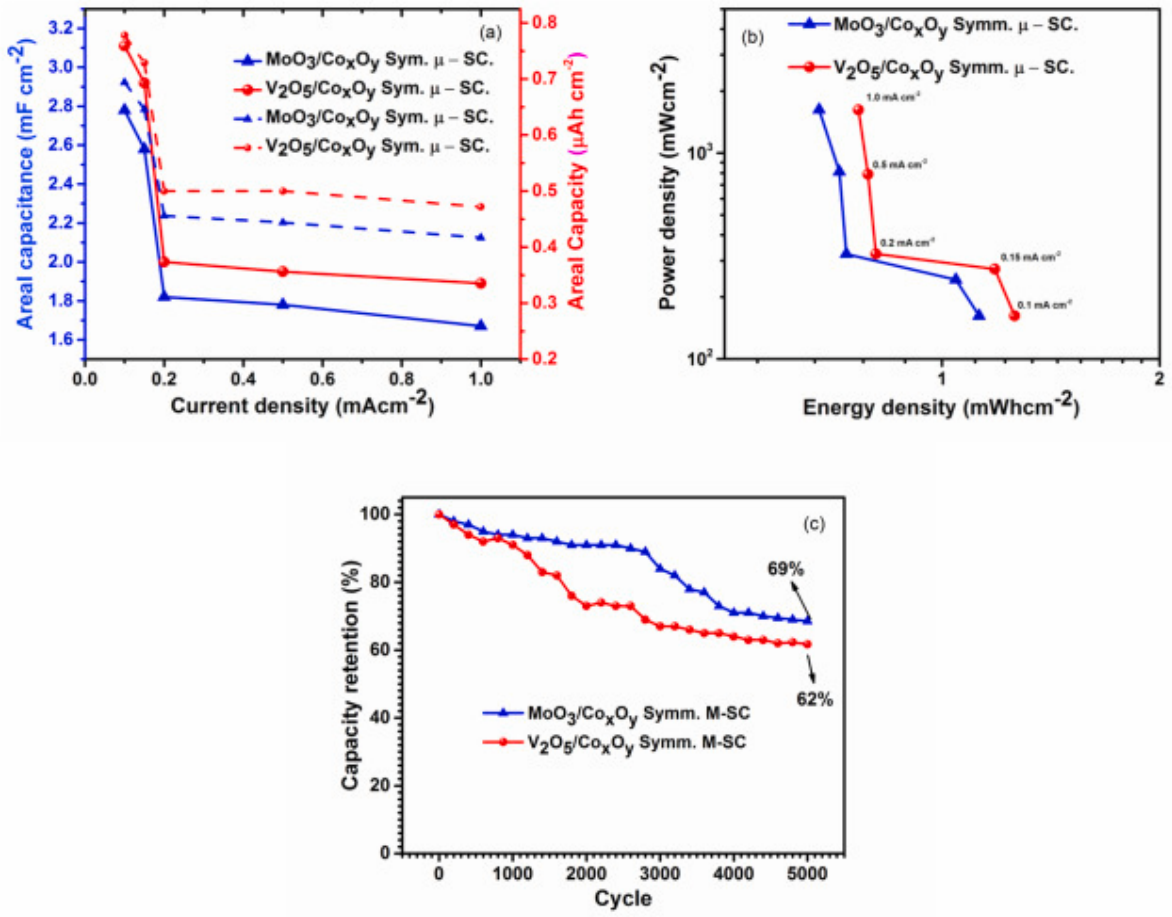

Fig. 9. (a) Areal capacitance/capacity as a function of current densities (b) Ragone plots and (c) Cyclic performance for the fabricated MoO_3/ Co_xO_y || MoO_3/ Co_xO_y and.

Plots of power density as a function of energy density (Ragone plots) for both μ-SC devices at current densities ranging from 0.1 to 1.0 mAcm^{-2}, are shown in Fig. 9(b). It can be seen from the curves that the devices maintained considerable drop in energy density from 1.13 to 0.68 μWhcm^{-2} and from 1.26 to 0.76 mWhcm^{-2} meanwhile there is a remarkable increase in power density from 162.57 to 1633.74 mWcm^{-2} and 159 to 1626.42 mWcm^{-2} for the $MoO_3/Co_xO_y||MoO_3/Co_xO_y$ and $V_2O_5/Co_xO_y||V_2O_5/Co_xO_y$ devices, respectively. The results compare to those obtained for NPG-MnO_2 nanowires and $V_2O_5||V_2O_5$ based μ-SCs [23,27]. This suggests that the power density of the fabricated μ-SCs can still go high at a considerable loss in stored energy. Interestingly, this result demonstrates high performance suggesting that the devices are developed from metal oxides which enhance

pseudocapacitance. It also corroborates effectiveness of μ-SCs over microbatteries where energy density becomes higher at significant detriment of the power density [17].

In order to investigate the stability of the $MoO_3/Co_xO_y||MoO_3/Co_xO_y$ and $V_2O_5/Co_xO_y||V_2O_5/Co_xO_y$ planar μ-SCs, charge/discharge tests were carried out at a constant current density of 1.0 $mAcm^{-2}$ for 5000 cycles. They are presented as the plots of capacity retention versus number of cycles in Fig. 9(c). The planar supercapacitors showed moderate cycling stability with 69 and 62% retention of initial areal capacitance for $MoO_3/Co_xO_y||MoO_3/Co_xO_y$ and $V_2O_5/Co_xO_y||V_2O_5/Co_xO_y$, respectively after 5000 cycles. This shows that $MoO_3/Co_xO_y||MoO_3/Co_xO_y$ cell has higher stability than $V_2O_5/Co_xO_y||V_2O_5/Co_xO_y$. In addition, gradual decrease in the initial areal capacitance value from first cycle to 5000th cycles with ~30% reduction for $MoO_3/Co_xO_y||MoO_3/Co_xO_y$ cell and ~40% reduction for $V_2O_5/Co_xO_y||V_2O_5/Co_xO_y$ cell is observed. This reduction may be attributed to dehydration of residual water content of the gel polymer electrolyte. These observations fall within some comparable values for planar thin film supercapacitors [5,25,27].

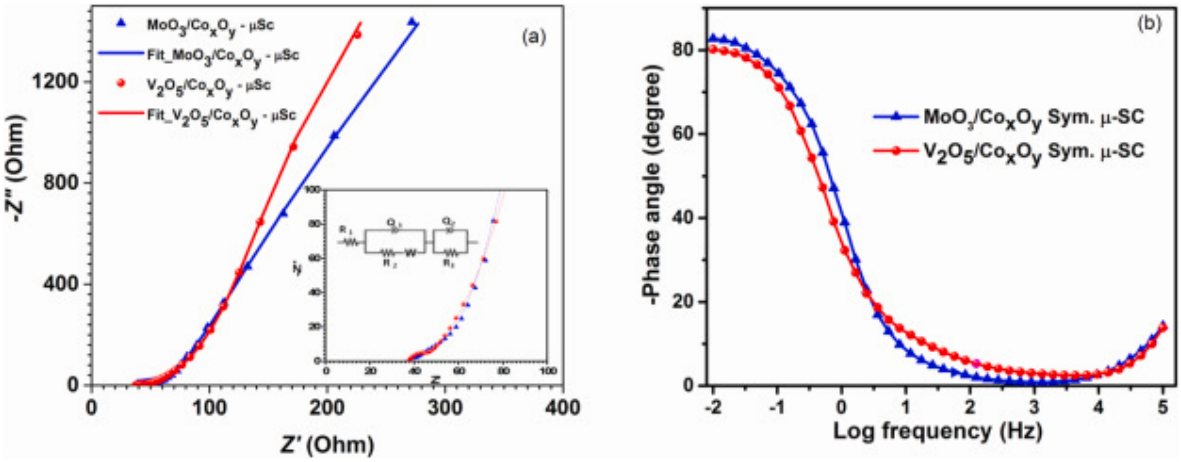

Fig. 10. (a) Nyquist EIS plots and fit, (b) Bode EIS plots of MoO_3/ Co_xO_y || MoO_3/ Co_xO_y and V_2O_5/ Co_xO_y || V_2O_5/v fabricated symmetric μ-

3.3.3. Electrochemical impedance spectroscopy (EIS)

Charge transfer kinetics and electrochemical behavior of the $MoO_3/Co_xO_y||MoO_3/Co_xO_y$ and $V_2O_5/Co_xO_y||V_2O_5/Co_xO_y$ planar μ-SCs were also investigated. Nyquist and Bode plots derived from the EIS measurements were fitted with the RC electric circuit using *Z*-fit software. The plots are shown in Fig. 10 (a and b), respectively. The fitted equivalent circuit consists of ohmic resistance R_1 which represents a combined resistance of ions, that of gel polymer electrolyte, the intrinsic resistance of current collector (ITO substrate) and the interface resistance of electrode materials and substrate [[17], [18], [19], [20], [21], [22], [23], [24], [25], [26], [27]]. The *Q* is a constant phase element related to the double layer capacitance and R_2 can be linked to the faradaic charge transfer resistance and transport which also occur at the electrode-electrolyte interface. Warburg element *W* represents the diffusion-controlled process that occurs in the electrode materials. It gives spike at low frequency towards high frequency of the plots [18,23,26]. R_1, R_2 and *W* were obtained from the fitted data and their respective values are 35.83 Ωcm^{-2}, 14.8 Ωcm^{-2} and 3.2 $k\Omega cm^{-2}$ for $MoO_3/Co_xO_y||MoO_3/Co_xO_y$ and 38.04 Ωcm^{-2}, 16.1 Ωcm^{-2} and 3.9 $k\Omega cm^{-2}$ for $V_2O_5/Co_xO_y||V_2O_5/Co_xO_y$ μ-SCs. From Bode plots, it can be observed that the cells demonstrated phase angle of ~80° at the low frequency region. The feature suggests pseudocapacitive response of the cells. The knee frequency (frequency at phase angle of 45°), which is the maximum frequency at which the pseudocapacitor optimally generates power were determined from the Bode plots for each cell. The results indicate knee frequency of $MoO_3/Co_xO_y||MoO_3/Co_xO_y$ cell (greater than 100 Hz) is larger than that of the $V_2O_5/Co_xO_y||V_2O_5/Co_xO_y$ (less than 10 Hz). Higher Knee frequency has been reported to corroborate

faster pseudocapacitive process of V_2O_5/Co_xO_y based device which in turn contributes to higher power density and capacity of the device [18].

4. Conclusion

All-oxide photovoltaic and symmetric interdigit device structures have been successfully developed from MoO_3, V_2O_5, and Co_xO_y. The samples were prepared using a home-made two electrode cell arrangement. The performances of the structures were evaluated from current density-voltage curves measured using AM1.5 G solar simulator. Increase in shunt resistances of the buffered cell implies that the buffer layers improve the performance of the photovoltaic cells. The measurements also provided for ITO|Co_xO_y|V_2O_5|Au cell with the highest power conversion efficiency of 0.39%. The efficiencies of these cells are comparable to some reports in literatures. Electrochemical measurements of the structures were investigated using a potentiostatic electrochemical workstation. The results reaffirmed the pseudocapacitive properties of the electrode materials and showed that for applications in electrochemical energy storage, the Co–V mixed oxide film is capable of delivering higher capacitive values and stability than Co–Mo's. The results also revealed comparable high areal capacitance, energy and power density values for both the MoO_3/Co_xO_y||MoO_3/Co_xO_y and V_2O_5/Co_xO_y||V_2O_5/Co_xO_y planar μ-SCs. EIS measurement shows that MoO_3/Co_xO_y||MoO_3/Co_xO_y has higher series resistance. The results can be used to suggest the application of nanostructured interfacial layers of V_2O_5/Co_xO_y and MoO_3/Co_xO_y as electrode materials in photovoltaic and energy storage devices. It also demonstrated the suitability of the materials for the development of high-performance nanostructured micro-made supercapacitors.

Author's statement

On behalf of all the authors, I thank you for speedy and thorough review of this manuscript. The comments of the reviewers are well appreciated and we believe they enrich the report. All the queries have been judiciously answered in fairness according to our findings of the research.

Declaration of competing interest

The authors declare that they have no known competing financial interests or personal relationships that could have appeared to influence the work reported in this paper.

Acknowledgments

The financial support of Osun State University, Osogbo, Nigeria through NEEDS Assessment Intervention fund with award number UNIOSUN/NEEDS/2019/0004 is gratefully acknowledged. S. A. Adewinbi is thankful to Dr. B. A. Taleatu of Obafemi Awolowo University (OAU), Ile-Ife Nigeria for his supervision and technical supports on the studies. He also gratefully acknowledges Prof. N. Manyala of the University of Pretoria (UP), South Africa for accessibility to UP research facilities.

References

[1] V. Vega-Garita, L. Ramirez-Elizondo, N. Narayan, P. Bauer, Integrating a photovoltaic storage system in one device: a critical review, Prog. Photovoltaics Res. Appl. 27 (4) (2019) 346–370.

[2] W.S. Ebhota, T.C. Jen, Efficient Low-Cost Materials for Solar Energy Applications: Roles of Nanotechnology in Recent Developments in Photovoltaic Materials and Devices, Intech Open, 2018.

[3] S. Calnan, Applications of oxide coatings in photovoltaic devices, Coatings 4 (1) (2014) 162–202.

[4] S. Pan, Z. Zhang, W. Weng, H. Lin, Z. Yang, H. Peng, Miniature wire-shaped solar cells, electrochemical capacitors and lithium-ion batteries, Mater. Today 17 (6) (2014) 276–284.

[5] C. Shen, X. Wang, S. Li, W. Zhang, F. Kang, A high-energy-density micro supercapacitor of asymmetric MnO_2–carbon configuration by using micro-fabrication technologies, J. Power Sour. 234 (2013) 302–309.

[6] S. Ruhle, A.Y. Anderson, H.N. Barad, B. Kupfer, Y. Bouhadana, E. Rosh-Hodesh, A. Zaban, All-oxide photovoltaics, J. Phys. Chem. Lett. 3 (24) (2012) 3755–3764.

[7] B.A. Taleatu, L. Cozzarini, B. Olofinjana, G. Bertolini, S.A. Adewinbi, S. Behrendt, Preparation of nanocrystalline ZnO/ Co_xO_y and CNT/ Co_xO_y bilayers for photoabsorption potential: XPS and some surface structural characterization, Mater. Sci. Semicond. Process. 87 (2018) 155–161.

[8] C.D. Lokhande, D.P. Dubal, O.S. Joo, Metal oxide thin film based supercapacitors, Curr. Appl. Phys. 11 (3) (2011) 255–270.

[9] D. Majumdar, T. Maiyalagan, Z. Jiang, Recent progress in ruthenium oxide-based composites for supercapacitor applications, Chem. ElectroChem. 6 (17) (2019) 4343–4372.

[10] S. Makino, Y. Yamauchi, W. Sugimoto, Synthesis of electro-deposited ordered mesoporous RuO_x using lyotropic liquid crystal and application toward micro-supercapacitors, J. Power Sour. 227 (2013) 153–160.

[11] D. Yang, Application of nanocomposites for supercapacitors: characteristics and properties, Nanocomposites-New Trends Dev. (2012) 299–328.

[12] S.A. Adewinbi, B.A. Taleatu, R.A. Busari, O.E. Adewumi, E. Omotoso, K. O. Oyedotun, N. Manyala, Preparation and surface characterization of nanostructured MoO_3/Co_xO_y and V_2O_5/ Co_xO_y interfacial layers as transparent oxide structures for photoabsorption, J. Electron. Mater. 49 (6) (2020) 1–12.

[13] G.J.J. Lof, L.J.A. Koster, Light Intensity Dependence of the Open-Circuit Voltage in Organic Bulk Heterojunction Solar Cells, 2014.

[14] K. Bouzidi, M.A.B.A. Chegaar, A. Bouhemadou, Solar cells parameters evaluation considering the series and shunt resistance, Sol. Energy Mater Sol. 91 (18) (2007) 1647–1651.

[15] B. Kupfer, K. Majhi, D.A. Keller, Y. Bouhadana, S. Rühle, H.N. Barad, A. Zaban, Thin film Co_3O_4/TiO_2 heterojunction solar cells, Adv. Energy Mater. 5 (1) (2015), 1401007.

[16] K. Majhi, L. Bertoluzzi, K.J. Rietwyk, A. Ginsburg, D.A. Keller, P. Lopez-Varo, A. Zaba, Combinatorial investigation and modelling of MoO_3 hole-selective contact in TiO_2| Co_3O_4| MoO_3 all-oxide solar cells, Adv. Mater. Interfaces 3 (1) (2016), 1500405.

[17] K.O. Oyedotun, M.J. Madito, D.Y. Momodu, A.A. Mirghni, T.M. Masikhwa, N. Manyala, Synthesis of ternary NiCo- MnO_2 nanocomposite and its application as a novel high energy supercapattery device, Chem. Eng. J. 335 (2018) 416.

[18] S.A. Adewinbi, B.A. Taleatu, R.A. Busari, V.M. Maphiri, K.O. Oyedotun, N. Manyala, Synthesis and electrochemical characterization of pseudocapacitive α- MoO_3 thin film as transparent electrode material in optoelectronic and energy storage devices, Mater. Chem. Phys. (2021), 124468.

[19] Y. Gao, S. Chen, D. Cao, G. Wang, J. Yin, Electrochemical capacitance of Co_3O_4 nanowire arrays supported on nickel foam, J. Power Sources 195 (6) (2010) 1757–1760.

[20] T. Nguyen, M. Boudard, M.J. Carmezim, M.F. Montemor, Layered $Ni(OH)_2$-Co $(OH)_2$ films prepared by electrodeposition as charge storage electrodes for hybrid supercapacitors, Sci. Rep. 7 (2017), 39980.

[21] C. Wu, L. Chen, X. Lou, M. Ding, C. Jia, Fabrication of cobalt-nickel-zinc ternary oxide nanosheet and applications for supercapacitor electrode, Front. Chem. 6 (2018), 597.

[22] B. Mendoza-S´anchez, T. Brousse, C. Ramirez-Castro, V. Nicolosi, P.S. Grant, An investigation of nanostructured thin film α- MoO_3 based supercapacitor electrodes in an aqueous electrolyte, Electrochim. Acta 91 (2013) 253–260.

[23] R. Velmurugan, J. Premkumar, R. Pitchai, M. Ulaganathan, B. Subramanian, Robust, flexible, and binder free highly crystalline V_2O_5 thin film electrodes and their superior supercapacitor performances, ACS Sustain. Chem. Eng. 7 (15) (2019) 13115–13126.

[24] J.K. Lee, G.P. Kim, K.H. Kim, I.K. Song, S.H. Baeck, Fabrication of mesoporous cobalt oxide (Co_3O_4) film by electrochemical method for electrochemical capacitor, J. Nanosci. Nanotechnol. 10 (5) (2010) 3676–3679.

[25] C.J. Raj, M. Rajesh, R. Manikandan, J.Y. Sim, K.H. Yu, S.Y. Park, B.C. Kim, Two-dimensional planar supercapacitor based on zinc oxide/manganese oxide core/shell nano-architecture, Electrochim. Acta 247 (2017) 949–957.

[26] C.J. Raj, M. Rajesh, R. Manikandan, W.G. Lee, K.H. Yu, B.C. Kim, Direct fabrication of two-dimensional copper sulfide nanoplates on transparent conducting glass for planar supercapacitor, J. Alloys Compd. 735 (2018) 2378–2383.

[27] J. Han, Y.C. Lin, L. Chen, Y.C. Tsai, Y. Ito, X. Guo, M. Chen, On-chip micro-pseudocapacitors for ultrahigh energy and power delivery, Adv. Sci. 2 (5) (2015), 1500067